

A Solenoidal Detector for Deeply Virtual Compton Studies at Luminosities $\geq 10^{37} / \text{cm}^{-2}\text{s}^{-1}$ and energies 6 – 12 GeV

Charles E. Hyde-Wright, Gail E. Dodge, Gagik
Gavalian, David Hayes, Lawrence B. Weinstein
Old Dominion University, Norfolk VA

Bernard Michel, Pierre-Yves Bertin
Université Blaise Pascal, Clermont-Ferrand, France

J. P. Chen, Eugene Chudakov, Bogdan Wojtsekhowski,
Sirish Nanda, Bodo Reitz, Robert Feuerbach, Javier Gomez
Jefferson Laboratory, Newport News, VA

Ron Gilman, Elena Kuchina
Rutgers University, New Brunswick, NJ

The Jefferson Lab Hall A Collaboration
(Dated: 6 December 2004)

We propose a solenoidal detector for exclusive electro-production reactions, particularly Deeply Virtual Compton Scattering (DVCS): $ep \rightarrow ep\gamma$ and Double DVCS $ep \rightarrow ep l^+ l^-$. The detector is built around a 1.1 m diameter, 1 m long, 2 Tesla solenoid, with a liquid hydrogen target at the upstream end of the solenoid. The downstream end-cap is instrumented for angles ≥ 100 milli-radians with a highly segmented high resolution total absorption calorimeter, for electron and photon detection. For scattering angles less than 45° , the barrel is instrumented with a Gas Electron Multiplier (GEM) based Radial Time Projection Chamber (RTPC) and with plastic scintillator for identification and tracking of the recoil protons. In addition to the calorimeter, the End-cap is also instrumented with a 10 cm deep TPC and a scintillator array for $e/\gamma/p$ discrimination. As an upgrade, the return yoke of the solenoid can be instrumented with coarse grained detectors for muon identification for coherent $J\Psi$ and di-lepton production studies.

We demonstrate that this detector can function at luminosities of at least $10^{37}/\text{cm}^2/\text{s}$. This will enable extremely high precision studies of many important exclusive reactions.

Contents

I. Introduction	3
A. Kinematics	4
B. Deeply Virtual Compton Scattering	5
C. Double DVCS	7
II. Detection Strategy	8
III. Detector Design Criteria	9
A. Magnetic Field	10
1. Møller Electrons	10
2. Target and Scattering Chamber	12
B. π^0/γ separation	13
C. Backgrounds	13
IV. Description of Solenoidal Detector	14
A. Solenoid	14
B. Particle ID	14
C. Calorimeter	15
D. Scintillator	15
V. Trigger	16
VI. Background Rates	17
A. Calorimeter	17
B. Scintillator	20
C. GEM based TPC	20
VII. Costs	22

A. TPC cost	22
B. Calorimeter	22
C. Solenoid	22
D. Scintillator	23
E. Electronics	23
VIII. Exclusivity	23
IX. Count Rates	24
A. DVCS	25
B. Charmonium	26
C. Conclusions	26
X. Bibliography	26
References	26

I. INTRODUCTION

Exclusive Deeply Virtual reactions provide access to a new class of observables, called Generalized Parton Distributions (GPDs) [1]–[9]. The GPDs offer us the unprecedented capability of constructing spatial images of the density of quarks inside the nucleon, as a function of the quark wavelength [7], [8], [9]. In this proposal we specifically consider the following reactions: Deep Virtual Compton Scattering (DVCS) $ep \rightarrow ep\gamma$; Deep Virtual π^0 Production $ep \rightarrow ep\pi^0$; Doubly Deep Virtual Compton Scattering (D²VCS) $ep \rightarrow e'pl^+l^-$, and exclusive J/Ψ electro-production.

The final state phase space of these reactions is complicated. The cross sections are also small: the DVCS cross section is $\mathcal{O}(\alpha^3)$ and the D²VCS cross section is $\mathcal{O}(\alpha^4)$. Thus high luminosity combined with high acceptance is essential. Previous proposals for studies of these reactions at 6–12 GeV at Jefferson lab have been designed around general purpose equipment. In this proposal we explore the feasibility of a specialized detector designed specifically for these reactions. Despite the technical challenges posed by these processes, we are motivated by the intuition that exclusive Deep Virtual processes offer a number of

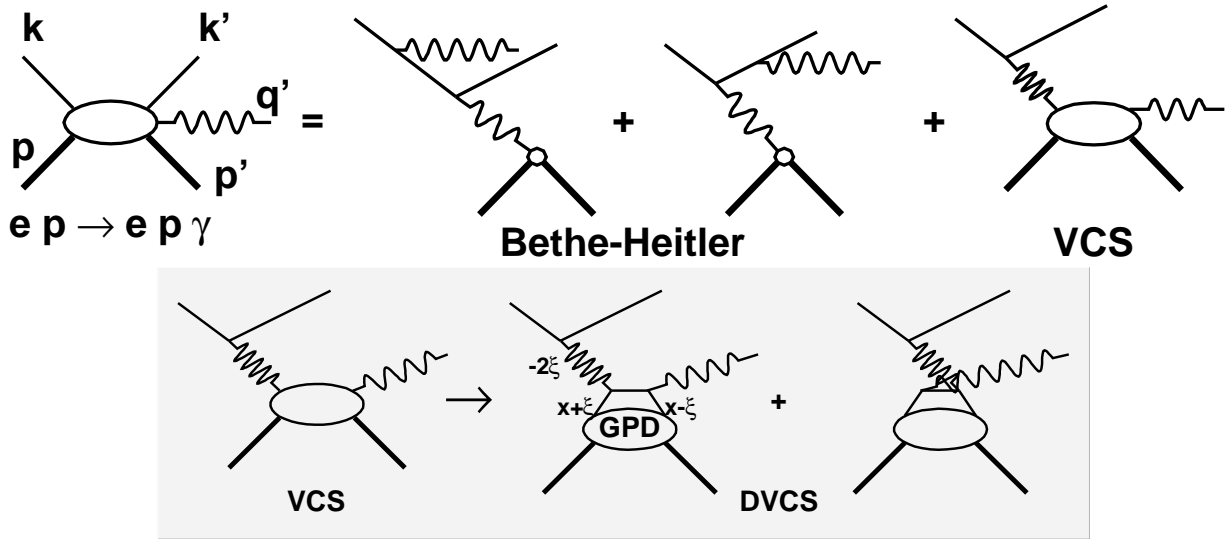


FIG. 1: Kinematics of the $eN \rightarrow eN\gamma$ reaction and the factorized DVCS amplitude. The kinematic invariants are $Q^2 = -q^2 = -(k - k')^2$, $x_{\text{Bj}} = Q^2/(2p \cdot q)$, $t = (q - q')^2$. In the Bjorken limit, the skewness parameter $\xi \rightarrow x_{\text{Bj}}/(2 - x_{\text{Bj}})$.

distinct advantages, which will permit a dedicated detector to be built at lower cost and operate at much higher luminosity than a general purpose apparatus.

The experimental simplifications of Deep Virtual reactions are straight forward. In the limit of modest momentum transfer to the recoiling nucleon (less than 1 GeV/c) almost the entire beam energy is deposited in either: two electromagnetic showers (DVCS); three electromagnetic showers ($ep \rightarrow epe^+e^-$); or one shower and two muons ($ep \rightarrow ep\mu^+\mu^-$). Thus very strong background rejection factors can be built into a hardware trigger. Secondly, because the proton recoil momentum is generally 1/10th beam momentum, the precision of measurement of the recoil proton can be roughly $10\times$ worse than the electron and photon, and still ensure exclusivity. Finally, since it is possible to measure all final state particles, the reaction is over-complete. Thus exclusivity of the reaction can be established even without measuring the magnitude of the momenta of all particles.

A. Kinematics

We define our kinematic variables for DVCS in Fig. 1. The skewness parameter is the light-cone momentum transfer fraction:

$$\xi = (q - q')^+ / (p + p')^+ \quad (1)$$

For D²VCS, the final photon q' is time-like, and materializes as a di-lepton pair of momentum $q' = k_+ + k_-$.

B. Deeply Virtual Compton Scattering

For DVCS, we consider the following kinematic bounds: $s > 4 \text{ GeV}^2$, $Q^2 > 2 \text{ GeV}^2$, $k' > 1.5 \text{ GeV}$. The bounds on s and Q^2 define the generally accepted region for inclusive deep inelastic scattering. The lower bound on k' is to ensure a clean separation between electromagnetic showers and minimum ionizing tracks in the calorimeter.

The kinematics at 11 GeV are illustrated in Fig. 2. The DVCS cross section is roughly proportional to the DIS cross section. For our initial design, we consider $\approx 30^\circ$ a reasonable upper bound for scattered electron detection, since the count rate is likely to fall rapidly at higher angles. However, we also consider options for calorimetry at larger angles because of the strong interest in achieving the highest possible Q^2 .

To avoid the high flux of Møller electrons, we do not instrument for angles smaller than 100 mr. In the target rest frame, the minimum momentum transfer to the proton $-t_{\min}$ is achieved with the outgoing photon parallel to the \vec{q} direction. DVCS events can be detected in kinematics with $\theta_q < 0.1$ rad with a loss of acceptance near the minimum momentum transfer. We note that

$$-t_{\min} \approx = \frac{x_{\text{Bj}}^2 M^2}{1 - x_{\text{Bj}} + M^2 x_{\text{Bj}}^3 / Q^2}$$

$$t_{\min} - t(\theta_{\gamma\gamma} = 0.1) \approx 0.1 \text{ GeV}^2. \quad (2)$$

The last formula indicates that for those kinematics with $\theta_q < 0.1$, the exclusion of photons in a cone of 100 mrad around the beam line introduces only a small shift in the minimum $-t$ accessible experimentally.

In the $ep \rightarrow ep\gamma$ reaction, the VCS amplitude interferes constructively with the Bethe-Heitler (BH) amplitude, in which the photon is radiated by the electron. At Jefferson Lab,

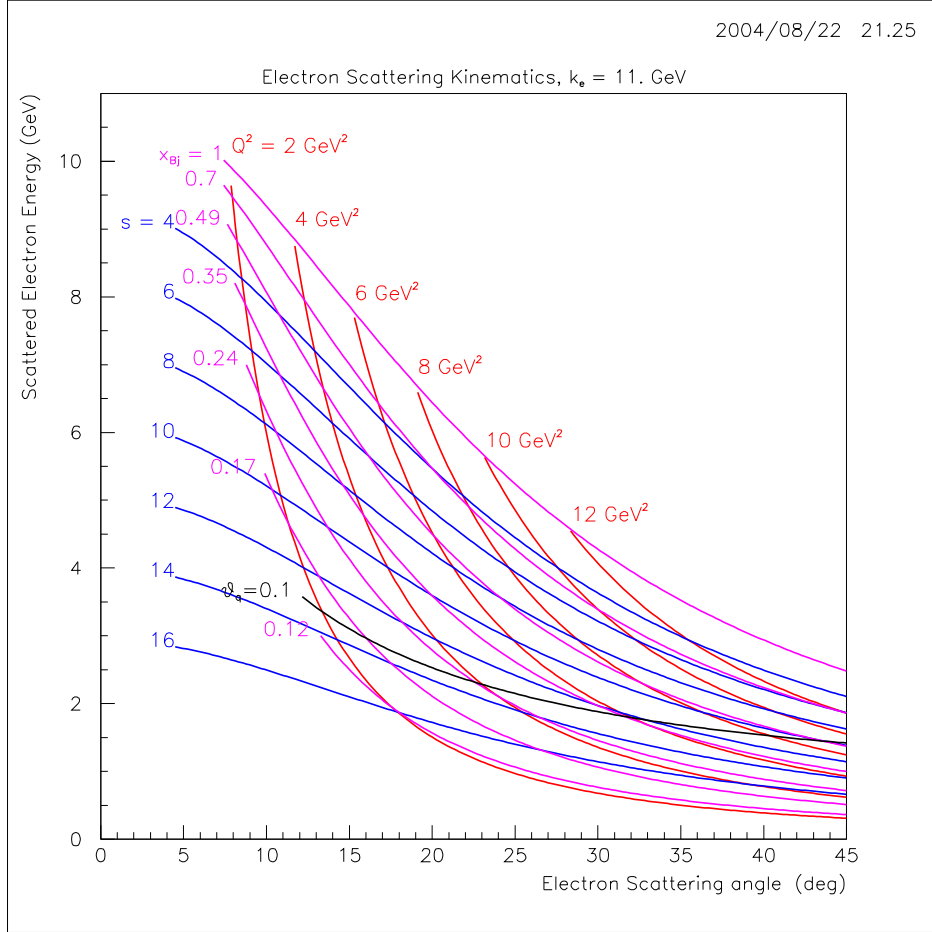


FIG. 2: Kinematics of DIS at 11 GeV. The practical kinematics is bounded above by the $s = 4$ GeV² line (blue), and on the left by the $Q^2 = 2$ GeV² line (red). Below the $\theta_q = 0.1$ rad line there is a loss of acceptance for DVCS at low $-t = (q - q')^2$, since the photon is no longer detectable exactly parallel to the \vec{q} . Also, it is desirable to have a high threshold (≥ 1.5 GeV) in the calorimeter for a trigger.

we use the BH amplitude as an amplifier and filter for the DVCS amplitude. One specific observable is the cross section difference for leptons of opposite helicities. In our kinematics, this cross-section difference is dominated by the interference of the imaginary part of the DVCS amplitude with a known BH amplitude. The full expression for the difference in the cross-section for leptons of opposite helicities is given by [5, 6]:

$$\frac{d^5\Sigma}{dQ^2 dx_B dt d\varphi} = \frac{d^5 \vec{\sigma}}{dQ^2 dx_B dt d\varphi} - \frac{d^5 \overleftarrow{\sigma}}{dQ^2 dx_B dt d\varphi} \quad (3)$$

$$= \frac{\alpha^3 (2-y)}{2\pi^2} \frac{1}{-t} \sqrt{\frac{K^2}{1+e^2}} \left[\frac{A \sin \varphi + B \sin 2\varphi + C \sin 3\varphi}{s'u'} \right]. \quad (4)$$

The variable φ is the azimuth of the hadron plane ($\vec{q}' \otimes \vec{p}'$) with respect to the electron scattering plane. The φ -dependent denominator $s'u' = -4(k \cdot q')(k' \cdot q')$ originates from the electron propagators of the BH process. $y = q \cdot p / k \cdot p$ is the invariant inelasticity and in the Bjorken limit the kinematic factor $K^2 / (1 + e^2) \rightarrow (1 - x_{Bj})(t_{\min} - t) / \vec{q}^2$. The $A \sin \varphi$ term is the leading twist contribution to the cross section difference. It is the sum of three (out of four) quark GPDs:

$$A = F_1(-t)\mathcal{H}(\xi, t) + \xi G_M(-t)\tilde{\mathcal{H}}(\xi, t) + \frac{-t}{4M^2} F_2(-t)\mathcal{E}(\xi, t), \quad (5)$$

$$\mathcal{H}(\xi, t) = \pi \sum_q e_q^2 [H_q(x = \xi, \xi, t) - H_q(x = -\xi, \xi, t)] \quad (6)$$

where F_1 , G_M , and F_2 are the usual elastic form factors, and the definitions of $\tilde{\mathcal{H}}$ and \mathcal{E} are analogous to Eq. 6. The $B \sin 2\varphi$ term in Eq. 4 is a higher twist term, and is therefore predicted to be suppressed by one power of $\sqrt{Q^2}$ relative to the leading twist term. The $C \sin 3\varphi$ term depends upon gluon helicity flip GPDs, and is expected to be much smaller than the other terms. Precise measurements of the Q^2 -evolution of A , B , and C are an important motivation for high statistics measurements of DVCS.

C. Double DVCS

In exclusive di-lepton pair production, factorization results from the large mass of the di-lepton pair. Thus we can study Inverse DVCS with real photons and D²VCS at $Q^2 \leq 1$ GeV². The imaginary part of the Double DVCS amplitude measures the Generalized Parton Distributions (GPD) at the kinematic point:

$$\begin{aligned} \Im [D^2VCS] &\propto GPD(\pm\eta, \xi, t) \\ \eta &\approx \frac{Q^2 - Q'^2}{2s + Q^2 - Q'^2} \\ \xi &\approx \frac{Q^2 + Q'^2}{2s + Q^2 - Q'^2} \end{aligned} \quad (7)$$

with $Q'^2 = q'^2$ the mass of the di-lepton pair. In Eq. 7 we have exchanged the definitions of η and ξ relative to Ref. [10], for consistency with our DVCS definitions. For $Q^2 < Q'^2$, D²VCS measures the $q\bar{q}$ region of the Generalized Parton Distributions. Thus these reactions

measure the quark content of the meson cloud, or penta-quark, structure of the nucleon. The imaginary part of the DDVCS amplitude is accessible experimentally by measuring single spin asymmetries. In the DDVCS case, we also have direct access to the Real part of the BH-DVCS interference, in a way that is only accessible in DVCS with the difference of electron and positron scattering. In the DDVCS case, at fixed Q^2 , Q'^2 , and t , the Real part of the BH*VCS interference is obtained from the asymmetry for $k_+ \leftrightarrow k_-$.

In inclusive Drell-Yan production in high energy hadron reactions, it is necessary to put a lower bound of 3 GeV on the di-lepton mass to remove the background of muons from hadronic decays, especially open charm. However, in the constrained kinematics of exclusive reactions these backgrounds disappear. The authors of [10] suggest that di-lepton masses above 1.5 GeV are sufficient for factorization in $\gamma p \rightarrow pl^+l^-$ [10]. At this scale, (comparable to baryon masses above 2 GeV, the usual criterion for DIS) the density of meson states is large enough to have confidence in duality. Fig. 3 illustrates sample di-lepton decay kinematics. We will present a more comprehensive analysis of this channel in a future update.

Figs. 2,3 illustrate that a maximum electron detection angle of 30° is a reasonable compromise for both DVCS and di-lepton detection. However, it is clear that larger detection angles are desirable for higher virtuality DVCS and higher mass IDVCS and D²VCS.

II. DETECTION STRATEGY

The Hall A DVCS experiments E00-110 and E03-106 measured the DVCS process with unshielded photon and proton detectors at a luminosity of 10^{37} . The minimum angle of a PbF₂ calorimeter block relative to the beam is $\approx 10^\circ$. The minimum angle of a proton detector element is 15° . In order to exploit the low- x_{Bj} region illustrated in Fig. 2, it is necessary to detect photons in a small cone around a virtual photon direction as close as 100 mr from the beam.

To cope with the flux of low energy Møller flux we propose to shield all detectors with a strong magnetic field. We believe this can achieve the combination of highest possible luminosity, large solid angle for the proton detection, small angle capability for the photon, and greatest flexibility for electron and photon detection. The luminosity is primarily limited by the flux of low energy charged particles and photons from the target. The large acceptance precludes shielding or a focussing spectrometer. A toroidal magnetic field requires a large

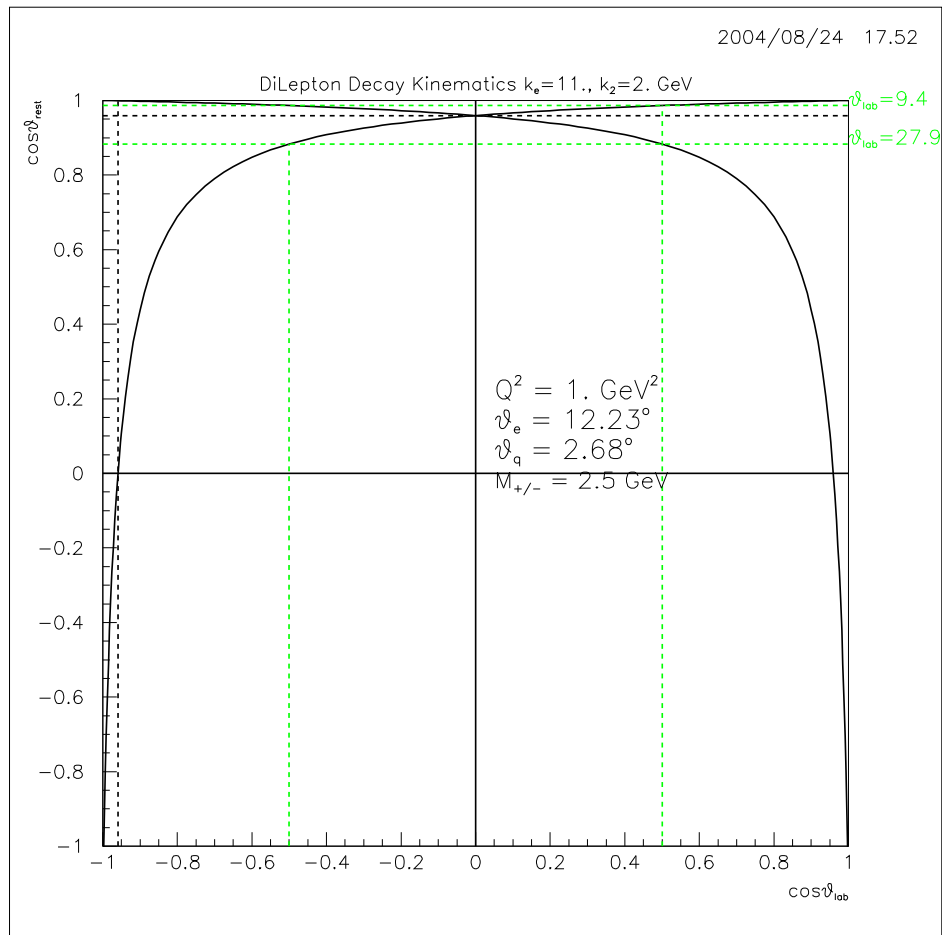


FIG. 3: Di-lepton decay kinematics for a 2.5 GeV mass di-lepton pair produced by a 9 GeV virtual photon ($Q^2 = 1 \text{ GeV}^2$). The ordinand is the cosine of the angle between the di-lepton momentum direction and the direction of one of the leptons in the pair, evaluated in the lab-frame. The abscissa is the same angle in the di-lepton rest-frame. The bounding angles of 9.4 and 27.9° contain 50% of the dilepton phase space.

sacrifice in acceptance for the coils and support structure. The detector design presented here, is modular and can be built in phases, to accommodate higher luminosity, higher acceptance, and an expanded physics program. We present the detector concept in Fig. 4. The following sections describe in more detail the performance criteria.

III. DETECTOR DESIGN CRITERIA

We consider a magnet-detector combination with the following capabilities.

- Electron and photon measurement from 0.1 rad to 30° , relative to the beam line.
 Angular resolution of 3 mr
 Energy resolution of $\sqrt{E}[3 - 5]\%$.
- Containment of the Møller electrons within the 0.1 rad cone.
- Luminosity of 10^{37} with a 1 cm long thin-walled LH_2 target.
- Detection of protons in cone from 0.1 rad to 45° , relative to beam line. Granularity of proton detector to be discussed later but much coarser than photon detection.
- Upgrade capability to muon detection
- Upgrade capability to electron detection at angles $30\text{--}45^\circ$. This is achievable by adding coarse grained Pb-Glass outside the Solenoid coil, with or without the Barrel scintillators replaced with a pre-radiator.
- Sufficient magnet field and tracking capability to track electrons sufficiently well to distinguish e^+/e^- .
- π^0 detection and γ/π^0 discrimination in DVCS kinematics.

We present the detector concept in Fig. 4. The following sections describe in more detail the and performance criteria.

If the photon is detected in a highly segmented calorimeter, a transverse resolution of 3 mm can be achieved. Thus the 3 mr angular resolution requirement places a minimum distance from target to calorimeter of 1 m. Without any tracking, a 1 cm long target contributes at most 1.25 mr to the angular resolution for electron scattering angles up to 30° .

A. Magnetic Field

1. Møller Electrons

At scattering angles above 0.1 radian, the maximum perpendicular momentum of electrons from Møller scattering is 10 MeV/c. In an axial magnetic field B , the radius of

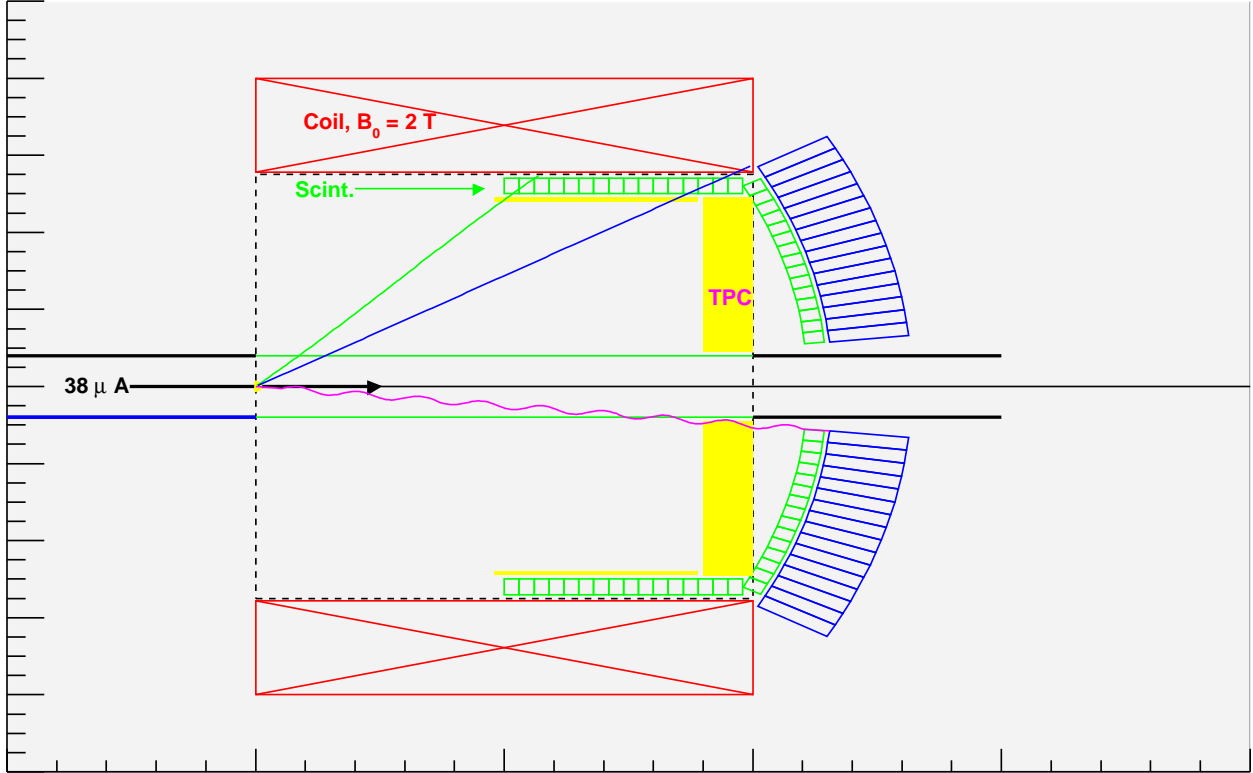


FIG. 4: Conceptual design for a high luminosity solenoidal detector for Deeply Virtual Compton Scattering. The solenoid is 1 m long with 1.1 m diameter inner bore. The target is at the upstream end of the solenoid. Electrons and photons are detected in the fine grained PbWO_4 calorimeter (blue). In front of the calorimeter, there is an array of plastic scintillators (green). The scintillators (together with the calorimeter) provide $e/\gamma/p$ separation. In front of the scintillators there is a 10 cm deep Time Projection Chamber (EndCap TPC). In the barrel region, there is a scintillator array (green) and a 1 cm deep Radial Time Projection Chamber – Barrel TPC (yellow). The wavy magenta line indicates a photon at the minimum angle of 100 mrad from the beam line. The blue and green lines indicate the helical trajectories of a 2 GeV/c electron and a 0.5 GeV/c proton emitted at 30° and 45° , respectively, from the beam line. The thin green lines parallel to the beam axis indicate a Be beam pipe.

curvature of the orbit helix is:

$$\begin{aligned}
 r_{\text{helix}} &= \frac{p_{\perp} c}{e B c} \\
 &= [3.33\text{m}] \frac{p_{\perp}}{1\text{GeV}/c} \frac{1\text{Tesla}}{B}
 \end{aligned} \tag{8}$$

To contain the Møller electrons within a beam pipe aperture defined by the 0.1 radian detection cone at a distance of 1 m from the target requires $r_{\text{helix}} < 5$ cm, or a magnetic field of 0.66 T. We have, however, chosen a central field of 2 T to give maximum flexibility in designing the scattering chamber, while minimizing low energy background in the detectors.

2. Target and Scattering Chamber

We choose a minimum electron energy to detect of 1.5 GeV, to ensure a large signal over background in the calorimeter. We also require less than 2 mr multiple scattering total in the target and exit beam pipe, or 1.4 mr in each. This defines a maximum material thickness:

$$\begin{aligned} X/X_0 &\leq [\theta_{ms} P_{\min} \beta / (15 \text{ MeV})]^2 \\ &= [1.4 \cdot 10^{-3} (1.5 \text{ GeV}) / (0.015 \text{ GeV})]^2 = 2\% \end{aligned} \quad (9)$$

The 2% radiation length puts an upper bound on a liquid hydrogen target ($X_0 = 61.3$ g/cm²) thickness of 17.4 cm. The target vacuum chamber can be either a spherical Al chamber mated to a downstream beam pipe or thin walled Be tube. For Al:

$$\begin{aligned} 2\% X_0(\text{Al}) &= 1.8 \text{ mm} \\ 2\% X_0(\text{Be}) &= 7.0 \text{ mm} \end{aligned} \quad (10)$$

Based on the Hall A DVCS scattering chamber, we expect a 35 cm radius Al shell can be made with a 1.8 mm wall thickness. Detailed background studies may allow a less stringent beam pipe design, but we assume the 0.1 r scattered electrons should pass through the hemispherical shell whereas the Møller electrons should be contained in a downstream beam pipe. At 35 cm (centered at the downstream end of a 10 cm target) the beam pipe must be ≤ 3.5 cm in radius. To contain the Møller electrons of $p_{\perp} \leq 10$ MeV within 3.5 cm, a magnetic field of 2 T is required. We will use this as the default magnetic field design. Beyond the end of the solenoid, the magnetic field on the axis decreases as $B_0/[1 + (z/r_S)^2]^{3/2}$. Thus for a 1 m long solenoid of radius $r_S = 0.55$ m, the Møller electrons remain contained within 100 mr for a distance 70 cm beyond the end of the solenoid.

The CMS detector at the LHC includes a 1 mm thick Be beam pipe, 8 cm in diameter with a total length of 1.5 m. If this is reduced to 1.0 m, and possibly smaller radius, this can achieve the 2% radiation length even for tracks at 100 mrad (0.7 mm radial thickness). This is clearly the more elegant solution:

- Reduced multiple scattering at large angles
- Completely open geometry at large angles for detector upgrades.
- Møller electrons contained with $B > 0.88$ T.
- Backgrounds at detector insensitive to target placement

B. π^0/γ separation

We assume that with fine grained calorimetry, double showers from π^0 decays can be resolved from γ showers if the transverse separation of the two showers exceeds twice the Molière radius r_M . For PbWO_4 , $r_M = 2$ cm. 50% of the π^0 decays occur with opening angles $[2 - (8/3)\sqrt{3}]m_\pi/E_p i$. The maximum exclusive photon or π^0 energy is 9 GeV (Fig. 2). π^0/γ resolution at this energy requires a flight path to the calorimeter of:

$$z > r_M E_\pi / m_\pi = 1.33m \quad (11)$$

If the calorimeter is placed at 1.1 m, the full π^0/γ separation is achievable up to $E_\pi = 7.4$ GeV

The size of the calorimeter is a dominant cost driver of this detector concept. We propose to place the calorimeter in a shell at radius 1.12 m. For the kinematics with $E_\pi > 7.4$ GeV, a dedicated run is required, with the target 25 cm upstream. This may increase the backgrounds slightly, if some of the Møller electrons shower in the downstream beam pipe. In this case, the magnetic field at the upstream target position will be ≈ 1.4 T. This is still sufficient to contain the Møller electrons.

Another option is to place the calorimeter 50 cm downstream of the solenoid. This significantly improves the γ/π^0 separation. In this case the calorimeter area expands by a factor of 2.25. However, with a Fe return yoke, this may allow the use of PMT, rather than Avalanche Photo Diode (APD) readout of the calorimeter blocks. This will substantially improve the energy resolution of the calorimeter. This option may also allow use of a common calorimeter for DVCS and the proposed Primakov program.

C. Backgrounds

In DVCS, the final state photon must be detected in a small cone around the virtual photon direction (typically < 200 mr half angle). However, the virtual photon direction itself is very close to the beam line, generally 100–200 mr. Conversely, the recoil protons, with momenta 400–1000 MeV/c must be detected in a cone of roughly 45° half angle around the beam line.

IV. DESCRIPTION OF SOLENOIDAL DETECTOR

A. Solenoid

The magnet is a 2 T solenoid, 1 m long and 1.10 m inner bore diameter. To facilitate an upgrade to include calorimetry at larger angles, the solenoid should be thin. Radial thicknesses less than one radiation length are possible. Many variations on the magnet are possible. Instead of a simple solenoid, the magnet could be segmented along the beam line, with a series of coils of increasing radius, to avoid the cost of the stored energy in the magnetic field at scattering angles $> 45^\circ$. Also, if the magnet is segmented in z (beam line) it may be possible to incorporate polarized targets with the detector.

B. Particle ID

A high granularity calorimeter can distinguish e/γ from protons, pions, muons, etc. The calorimeter also measures transverse position to 3mm and energy to $1\% \oplus 3.5\% \sqrt{E(1 \text{ GeV})}$.

Coarse grained tracking detectors inside and behind a Fe return yoke can identify muons for a exclusive di-lepton experiment. Factorization requires highest possible s and di-lepton mass. Thus typical di-lepton energy will be ≥ 8 GeV, and to detect both leptons, the decay phase space will be limited to leptons from 1/4 to 3/4 of the total di-lepton energy. Thus the minimum muon momentum to detect is 2 GeV, and one of the two muons will always have momentum above 4 GeV. With an absorber thickness of three hadronic interaction lengths (the calorimeter is ≈ 1 interaction length) a μ/π resolving power of 20/1 can be achieved. Since two particles must be identified, a $\pi^+\pi^-$ rejection factor of 400:1 can be achieved with a μ -counter upgrade.

A thick scintillator (> 4 cm) can resolve high energy hadrons (especially the recoil protons) from low energy photon background (97% below 3 MeV). Either this scintillator, or a gas chamber can discriminate between electrons and γ -rays. A 4 cm scintillator has a 7.5% probability of converting a high energy γ -ray to a signal \geq half of minimum ionizing. Thus without the TPC in front of the calorimeter, there would be a 7.5% event sample with ambiguous e/γ I.D.

C. Calorimeter

PbF_2 is a high density Cerenkov medium. It offers the best combination of high resolution and neutron/hadron immunity (except minimum ionizing signals). The E00-110 collaboration measured a resolution of $\sigma_E/E = 3\%/\sqrt{(1 \text{ GeV})E}$ with a test array. The cost of the E00-110 132 element array is \$800/crystal ($3 \times 3 \text{ cm}^2 \times 20X_0$). Total cost of crystals + PMT + Base+ cable approx \$2000/channel. To completely instrument the calorimeter EndCap requires 840 crystals for a total calorimeter cost estimate of \$1.7M.

Although there may be a magnetic field solution with the calorimeter outside the field region, we consider that the calorimeter probably requires Avalanche Photo Diode (rather than PMT) readout.

APDs have a very high quantum efficiency (75%, but also high cost per surface area. Thus APDs have been more commonly used with PbWO_4 calorimeters. PbWO_4 is a scintillator with light emission ≥ 200 photons/MeV with 90% of light emitted within 100 ns. The Hall B DVCS calorimeter couples APDs (5mm)² to the back face (15 mm)² of PbWO_4 crystals. The unit cost of crystal, APD, and pre-amp is approximately \$500. This corresponds to the same unit cost \$2000 per (3 cm)² surface as the quoted above for PbF_2 PMT combination. However, the Lead-Tungstate option requires four times the readout channels, unless multiple channels are summed together in the pre-amp stage. The total yield for PbWO_4 coupled to APDs is ≥ 2 photo-electrons/MeV. The Hall B Primakov experiment achieves higher yields with PbWO_4 coupled to PMTs.

D. Scintillator

Following the lead of E00-110, we consider that a coarse grained scintillator array is sufficient to identify the protons with sufficient angular resolution to resolve the exclusive channel. We consider an array of scintillator tiles of depth 4 cm, and $(3 \text{ cm})^2$ granularity matching the calorimeter blocks. Because the scintillators are in the magnetic field, they must be read out either by Avalanche Photo-Diodes, or wave shifting fibres to [multi-channel] PMTs. If the Visible Light Photon Detector (VLPC) technology is implemented at JLab, as planned for the Hall D Start-Counter, then this technology could be used with wave shifting fibres.

V. TRIGGER

The trigger is based on energy deposited in one or more showers in the calorimeter. We assume the calorimeter is digitized by a 100 MHz pipeline ADC. We also require parallel trigger logic that in real time can find local clusters in the calorimeter and in real time compute approximate shower energy and Q^2 (assuming the particle is an electron). The E00-110, E03-106 DVCS experiments in Hall A used a non pipeline version of this trigger logic, which summed all groups of four adjacent blocks to find showers above threshold. We present a schematic of the trigger logic in Fig. 5. For DVCS events, in this proposal we require two showers in the calorimeter, both with energy above 1.5 GeV, and at least one with $Q^2 > 1.5 \text{ GeV}^2$. We do not require both candidate showers to correspond to Q^2 above threshold, because for real DVCS events we generally expect a small angle high energy photon. When this photon is interpreted as an electron by the trigger logic, this will produce a small Q^2 value. To additionally restrict the random coincidence rate, we require that the sum energy of the two showers lies between 75% and 125% of the beam energy. Angular correlations could be used to further reduce the accidental rate.

The integrated inclusive $H(e, e')X$ cross section is $0.2 \mu\text{b}$ for $k' > 1.5 \text{ GeV}$, and $0.08 \mu\text{b}$ with the additional restriction $Q^2 > 1.5 \text{ GeV}^2$. With a 10 ns resolving time, the random trigger rate (luminosity $\mathcal{L} = 10^{37}/\text{cm}^2/\text{s}$) is less than 2 kHz. This is obtained for two DIS events above 1.5 GeV energy and at least one with $Q^2 > 1.5 \text{ GeV}^2$ and with energy sum between 75% and 125% of the 11 GeV beam energy.

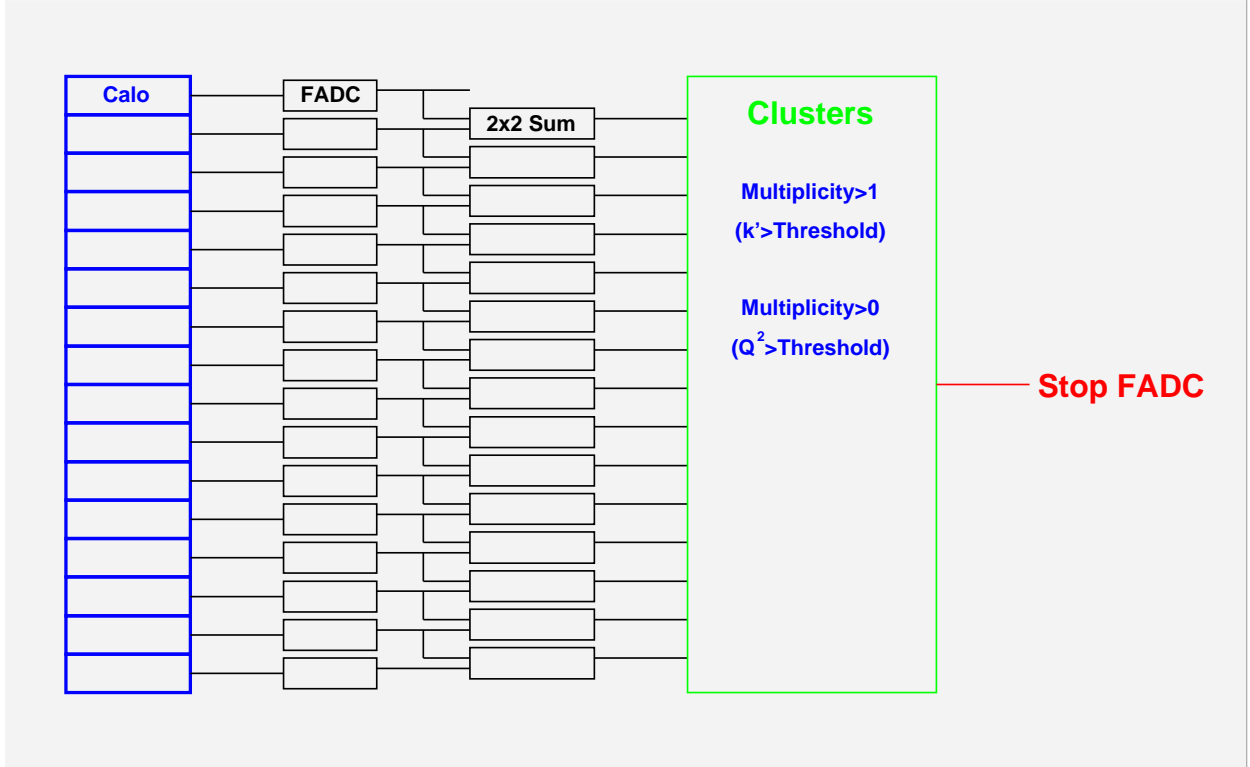


FIG. 5: Schematic DVCS Trigger Logic

VI. BACKGROUND RATES

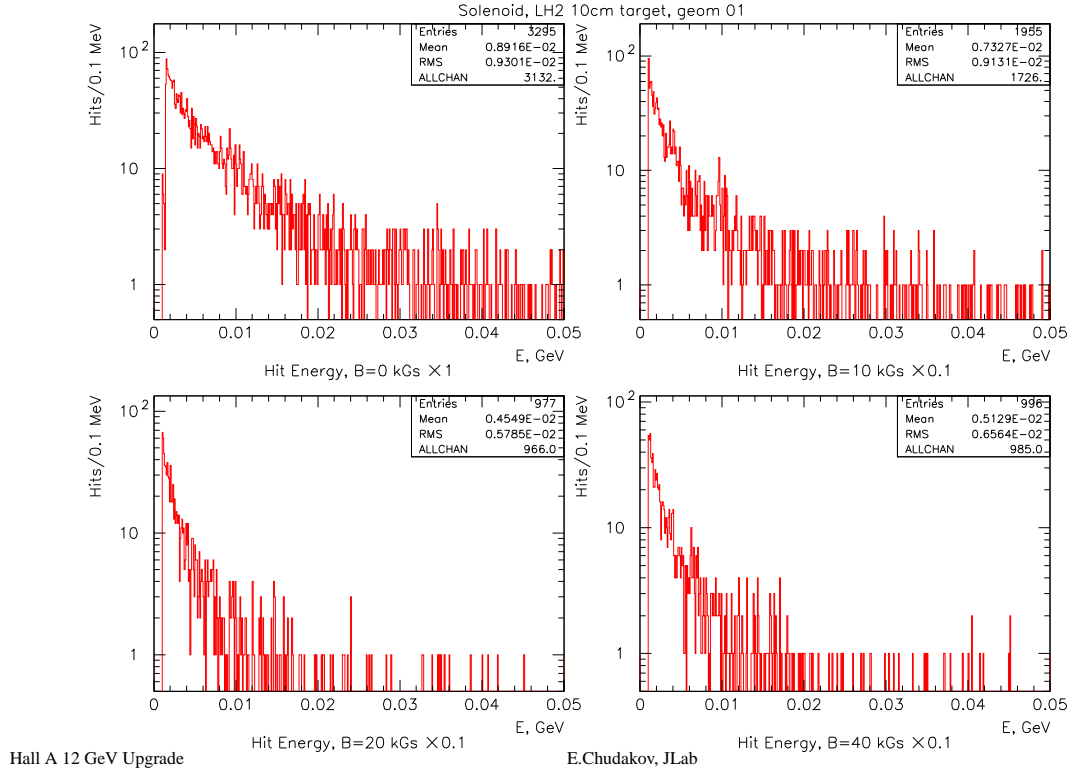
The total hadronic production rate $ep \rightarrow X$ is approximately 100 MHz (at $\mathcal{L} = 10^{37}/\text{cm}^2/\text{s}$). This is obtained from the quasi-real photon flux ($\approx 0.02/k_\gamma$ per electron) integrated over the photo-absorption cross section. This is much higher than the DIS inclusive rate, and will contribute to the trigger rate primarily via random (and real) coincidences of photons from two energetic neutral pions. The hadronic production rate drops to 25 MHz if we only consider events above the threshold to create a 3 GeV π^0 , guaranteed to produce at least one 1.5 GeV photon. We note however, that high energy photo-absorption generally has a high multiplicity of lower energy particles. We will continue to study the impact of this background on the trigger.

In the remainder of this section, we consider the impact on our detectors of the low energy background from atomic processes.

Solenoid detector GEANT simulation

Energies of hits in calorimeter

2004/09/01 21.02



2

FIG. 6: Energy distribution of electromagnetic background at downstream end-cap of 1 m long Solenoid. The distributions integrate over the radial coordinates $r > 10$ cm. The four panels are for central magnetic fields of 0 T (upper left), 1 T (upper right), 2 T (lower left), and 4 T (lower right)

A. Calorimeter

Figs. 6 and 7 present a GEANT study of the electron and photon backgrounds at the Solenoid end-cap, as a function of central magnetic field in the solenoid (www.jlab.org/~gen/jlab12gev/talk_sol_prel.pdf). For axial fields above 1 T, we find a power flux P a distance R from the axis, at a distance 1 m downstream of 10 cm LH₂

Solenoid detector GEANT simulation

Radial distribution of energy flux

2004/09/15 20.58

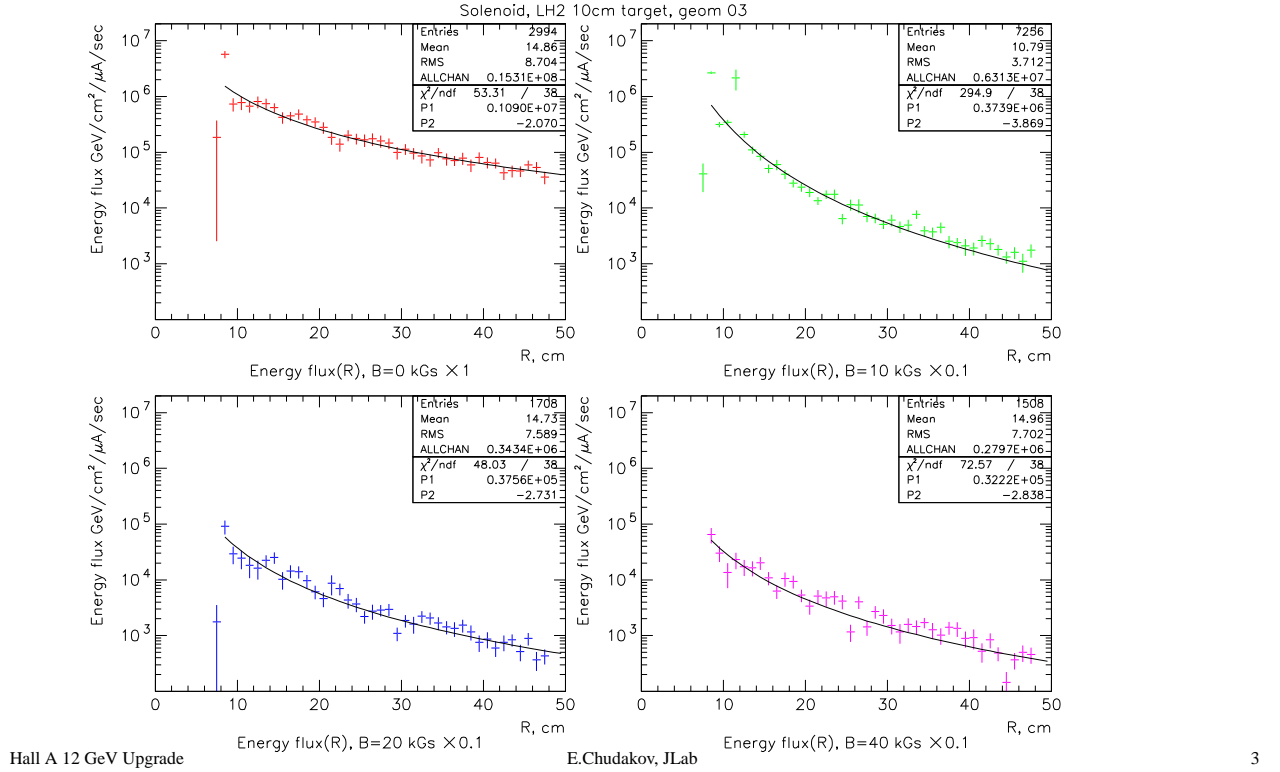


FIG. 7: Radial distribution of electromagnetic background at downstream end-cap of 1 m long Solenoid. The four panels are for central magnetic fields of 0 T (upper left), 1 T (upper right), 2 T (lower left), and 4 T (lower right). The plots are of energy flux in $\text{GeV}/\text{cm}^2/\mu\text{A}/\text{sec}$ as a function of radial distance from the beam line, 1 m downstream from the upstream end of a 10 cm liquid H_2 target. The curves are fits of the form $A \cdot [R/(10\text{ cm})]^\beta$. At $B = 2\text{ T}$, the fit parameters are $A = 3.0 \cdot 10^4\text{ GeV}/\text{cm}^2/\mu\text{A}/\text{sec}$ and $\beta = -2.5$.

target (upstream end):

$$P/I = \left(3.0 \cdot 10^4 \frac{\text{GeV}}{\text{cm}^2 \text{ s}}\right) \left(\frac{R}{10\text{ cm}}\right)^{-2.5} \text{ per } \mu\text{A} \text{ at } 1\text{ m} \quad (12)$$

$$\frac{P}{\mathcal{L}} = \frac{11\text{ MeV}}{\text{cm}^2(100\text{ ns})} \left(\frac{R}{10\text{ cm}}\right)^{-2.5} \text{ per } [10^{37}\text{ cm}^2/\text{s}] \quad (13)$$

For each calorimeter detector element of $3 \times 3 \text{ cm}^2$ at 1.12 m, the power flux for the innermost elements at $\mathcal{L} = 10^{37}/\text{cm}^2/\text{s}$ is 82 MeV per 100 ns. The energy spectrum of these photons is roughly $1/E_\gamma^2$, with 30% of the power flux from 100 KeV to 1 MeV. Photons below 100 KeV will likely be absorbed by the vacuum window. Given the large number of low energy photons, the fluctuations in this pile-up energy are likely to be much smaller than the average energy.

Assuming this low energy background is absorbed in the first 1 cm of calorimeter of density 8 g/cm^3 , then the radiation dose of the innermost detectors at $\mathcal{L} = 10^{37}/\text{cm}^2/\text{s}$ is 0.16 rad/s. Studies of radiation damage in PbWO_4 showed up to factor of two reduction in light output for doses of 1 kRad, but then stable up to 1 MRad. Radiation damage is a serious issue facing the performance of the central detector elements. However, the detector can function with high performance for a run of at least 3 months at 10^{37} . Thermal annealing for 2 hr at 200 C or optical bleaching (12 hr, $\lambda > 600\text{nm}$) will restore 3/4 of the radiation damage.

B. Scintillator

The recoil protons in exclusive deeply virtual reactions range in momenta from the minimum momentum $\sim x_{\text{Bj}}M$ ($p_{\text{min}} \approx \sqrt{-t}$, see Eq. 2) to $\sim 1 \text{ GeV}/c$. Thus the protons vary from heavily ionizing to nearly minimum ionizing. A 4 cm thick scintillator will produce 8 MeV signals from minimum ionizing tracks. A pulse threshold of 3 MeV above any DC background will discriminate between proton and low energy photon signals. The following rates apply to a proton scintillator array of the same granularity ($3 \text{ cm} \times 3 \text{ cm}$ at 1.12 m) as the calorimeter. Above 10 MeV, the photons convert via e^\pm conversion. This produces a rate of 0.8 MHz above 3 MeV in the inner most detectors. At lower energy, the absorption cross section rises and is dominated by the compton process. These compton events produce an additional 1.2 MHz above threshold, for a total rate of 2 MHz.

We assume all channels are converted with flash ADCs. If the effective integration/discrimination time for a PMT pulse from the scintillator is 20 ns, the accidental rate per channel is 1%. Beyond 250 mrad from the beam line (14.3°) the backgrounds have fallen by an order of magnitude.

Scintillator pads of this geometry ($3 \times 3 \times 4 \text{ cm}^3$) can be readout either by Avalanche

Photo Diodes (APD) or wave-shifting fibres to position-sensitive PMTs outside the magnetic field. If a PbWO_4 calorimeter is used (rather than a Cerenkov medium such as PbF_2) the scintillator array may be redundant – the protons will be detected in the PbWO_4 array. But either the scintillator or TPC is still needed for e/γ discrimination

For angles above 35° , although the distance from the target shortens to 0.7 m at 45° , the flux is more than 100 times lower than at 100 mrad.

C. GEM based TPC

A Gas Electron Multiplier (GEM) based Time Projection Chamber (TPC) in front of the end-cap (EndCap TPC) and the Radial TPC inside the barrel (Barrel TPC) serve the following functions:

- Improved e/γ separation;
- Tracking for vertex reconstruction with thick targets;
- Separately identify the positive and negative leptons in di-lepton production.
- Momentum resolution for the proton, or at least correction for the helical trajectory in solenoidal magnetic field.

In the forward direction, a 10 cm thick gas volume is sufficient. At 100 mrad, a track would cross at least 1 cm of the end-cap. The entrance foil to a TPC has minimum thickness $100 \mu\text{m}$, or $X/X_0 = 2.5 \cdot 10^{-4}$. The radiation length of this gas is comparable to the entrance window. At 1 m from the target, the conversion yield of soft photons into the TPC is 0.2 MHz per cm^2 at an angle of 100 mrad and a luminosity of $10^{37}/\text{cm}^2/\text{s}$. Again, this flux falls by a factor of 10 at 250 mrad. This rate can be further reduced in analysis, because roughly half of these tracks will originate inside the gas volume, and also the secondary electrons will follow very tight helices ($< 1 \text{ mm}$), rather than the straight tracks of multi-GeV/c particles.

A 10 cm thick TPC will have a residence time of up to $2 \mu\text{s}$, depending on the drift gas. A 10% occupancy in $2 \mu\text{s}$ per readout channel requires a pixel area $\leq 25 \text{ mm}^2$ at the inner radius, growing to 14 cm^2 at the outer radius of the EndCap TPC. Recently, 2D readout of strips has been achieved in GEM detectors with $400 \mu\text{m}$ pitch strips[12]. In this geometry, the second coordinate is capacitively coupled to the first, resulting in a very high correlation

(6.8% σ) between the charge readout on the two strips. This fluctuation in this correlation is much smaller than the intrinsic fluctuations in the Landau ionization distribution. This correlation can be used to resolve the ambiguity of multiple hits, without a third stereo coordinate.

As we discuss below in the Exclusivity section, it is much more important to measure the azimuthal, rather than radial, coordinate and slope of the track. Our preliminary design for the readout of the EndCap TPC includes two rings of radial strips: 1200 strips in radius from 10 to 17.5 cm, and 1200 strips from 17.5 cm to 50 cm. These strips have a transverse size of 0.52 mm at the inner radius, and 2.6 mm at the outer radius of 50 cm. In addition, there are an additional 2400 strips in thin rings around the beam axis. At the inner radius, these azimuthal strips are 0.48 mm wide and the annulus is divided into 12 sectors. At the outer radius, the azimuthal strips are 2.7 mm wide and the annulus is divided into 6 sectors. This is a total of 4800 pads in the EndCap TPC. For the Barrel TPC, we assume a readout granularity of $\approx 5 \text{ cm}^2$, for a total of 3000 readout channels. We do not need crossed strips in the Barrel. The Barrel TPC has a drift time of 200 ns (1 cm drift distance). Thus the occupancy in the Barrel TPC will be a factor of 10 lower than in the EndCap TPC.

We are also considering an alternate scheme for the EndCap tracking, with several separated planes of detectors. This would increase the total number of channels, but simplify the readout requirements.

VII. COSTS

A. TPC cost

GEM foil cost for BoNuS is \$300 per foil, maximum size = 40 cm \times 40 cm. 8–10 foils will cover EndCap, with radius 50-65 cm. At most 20 more to cover 60cm longitudinal of barrel. Maximum GEM foil cost is $30 \times \$300 = \$9K$.

Front-End electronics cost for BoNuS is \$20/channel, for a total of \$200K for front-end electronics.

B. Calorimeter

The calorimeter costs were already detailed above. The EndCap calorimeter cost is \$1.7M.

C. Solenoid

For a pure solenoid, the Particle Data Group web page (pdg.lbl.gov) gives the following scaling law for the cost of a superconducting solenoid:

$$\text{Cost} = \$0.523M(\mathcal{E}/1MJ)^{0.662} \quad (14)$$

where \mathcal{E} is the stored magnetic energy. This includes Cryostat, support and superconducting cable, but not the power supply. JLab already has an adequate supply of superconducting cable. For a solenoid of radius $R = 0.55$ m, Length $L = 1$ m, and field $B = 2$ T,

$$\mathcal{E} \approx \frac{\pi}{2\mu_0} B^2 R^2 L = 10^7 A^2 / J \left(\frac{1.2T^2 m^3}{8} \right) = 1.5MJ \quad (15)$$

$$\text{Cost} = \$0.68M \quad (16)$$

D. Scintillator

Scintillator costs are \$40 per $3 \times 3 \times 4$ cm³ scintillator (Eljen Technology estimate) and \$250/channel for APD readout Fibre readout to multi-anode PMT or VLPC may be less expensive. Total cost is \$290 per channel. For the EndCap array, the total cost is \$250K. For the Barrel array, the total cost is \$500K. However, since the cost is dominated by the light detector/readout, the cost can be reduced by a factor of two if the granularity in the barrel is decreased to 5×5 cm².

E. Electronics

The total number of channels proposed is:

- Calorimeter: 3400 (if no ganging of APDs is done)
- TPC: 7800

- Scintillator: 2600 (without any reduction of granularity of barrel).

Total number of channels is 13,800, dominated by the TPCs.

VIII. EXCLUSIVITY

Due to the difficulty of achieving high resolution and large solid angle detection, it is generally necessary to measure all final state particles in over-complete kinematics. Specifically, the DVCS reaction is 5-fold differential (before considering radiative tail effects). Thus measuring the directions of all 3 final particles overdetermines the reaction without any measurement of the energies. Stated another way, if the direction cosines of the 3-momentum vectors of the final electron, proton, and photon are measured, then 3-momentum conservation determines the 3-momenta of all three particles. The validity of energy conservation in this kinematics becomes a test of the exclusivity of the reaction.

We assume 3 mm (σ) transverse spatial resolution for the photons and electrons. For the proton detection, the resolution is the granularity of the scintillator array, or $4/\sqrt{12} \approx 1$ cm σ . The calorimeter energy resolution is sufficient to correct for the electron trajectories in the magnetic field to within the 3 mm precision. For di-lepton production, however, the tracking must resolve the sign of particle charge. This requires resolving the transverse derivative.

For the sake of discussion, we consider a uniform magnetic field in the solenoid. Then for a track of momentum p emitted with polar and azimuthal angles θ_0 and ϕ_0 (relative to the beam axis- z), the radial and azimuthal coordinates as a function of z are:

$$r(z) = 2r_0 \sin(\psi/2) \tag{17}$$

$$\phi(z) - \phi_0 = \psi(z)/2 \tag{18}$$

$$\psi(z) = \frac{z}{r_0} \tan \theta_0 \tag{19}$$

$$r_0 = \frac{p_{\perp} c}{eBc} = \frac{pc \sin \theta_0}{eBc} \tag{20}$$

For particles of interest that reach the EndCap TPC, the change in the azimuthal impact point is much greater than the change in the radial impact. In the EndCap TPC of depth Δz , the particle makes a track segment with the following radial and azimuthal coordinates:

$$\Delta z \frac{dr}{dz} = \Delta z \tan \theta_0 \cos(\psi/2) \tag{21}$$

$$\Delta z r \frac{d\phi}{dz} = \Delta z \tan \theta_0 \sin(\psi/2) \quad (22)$$

For the protons, the combined measurement of the impact (r, ϕ) and the azimuthal slope $r[d\phi/dz]$ is sufficient to reconstruct the vertex coordinates (θ_0, ϕ_0) . For di-lepton production, the sign of the slope $r[d\phi/dz]$ resolves the charge.

The reconstruction of exclusivity is represented in Fig. 8. In this figure, an ensemble of exclusive $ep \rightarrow ep\gamma$ and inclusive $ep \rightarrow eN^*\gamma$ events were generated. For the exclusive events, the event sample from Fig. 9 is used. After accounting for detector resolution (and N^* decay), the energies of all three particles (electron, gamma, proton) are calculated from just the measurement of the direction cosines of each particle with respect to the three Cartesian axis, and the assumption that the event is exclusive (including the N^* events). The plot in Fig. 8 is the missing energy, $k_e + M - k' - q' - E_p$, with all values in the final state reconstructed.

IX. COUNT RATES

We present some illustrative projections of the physics results that can be obtained with this detector.

A. DVCS

Fig. 9 illustrates the DVCS kinematics at $s = 10 \text{ GeV}^2$ and $Q^2 = 6 \text{ GeV}^2$ ($x_{\text{Bj}} = 0.4$) at 11 GeV. In Fig. 10 we show projected results for the helicity correlated cross section at this kinematic point. In Fig. 11 we show projected results for the helicity correlated cross section at $s = 14 \text{ GeV}^2$ and $Q^2 = 4 \text{ GeV}^2$ ($x_{\text{Bj}} = 0.23$). The suppression of the signal near $\phi = 0, 360$ is an acceptance effect from the small central angle (-5°) of the virtual photon direction.

B. Charmonium

Coherent J/Ψ production is the cleanest observable we have for accessing the gluon GPDs. The existing, exclusive J/Ψ photo-production data near threshold are consistent with a 2-gluon exchange model. At low Q^2 , this detector will produce 100 tagged J/Ψ per

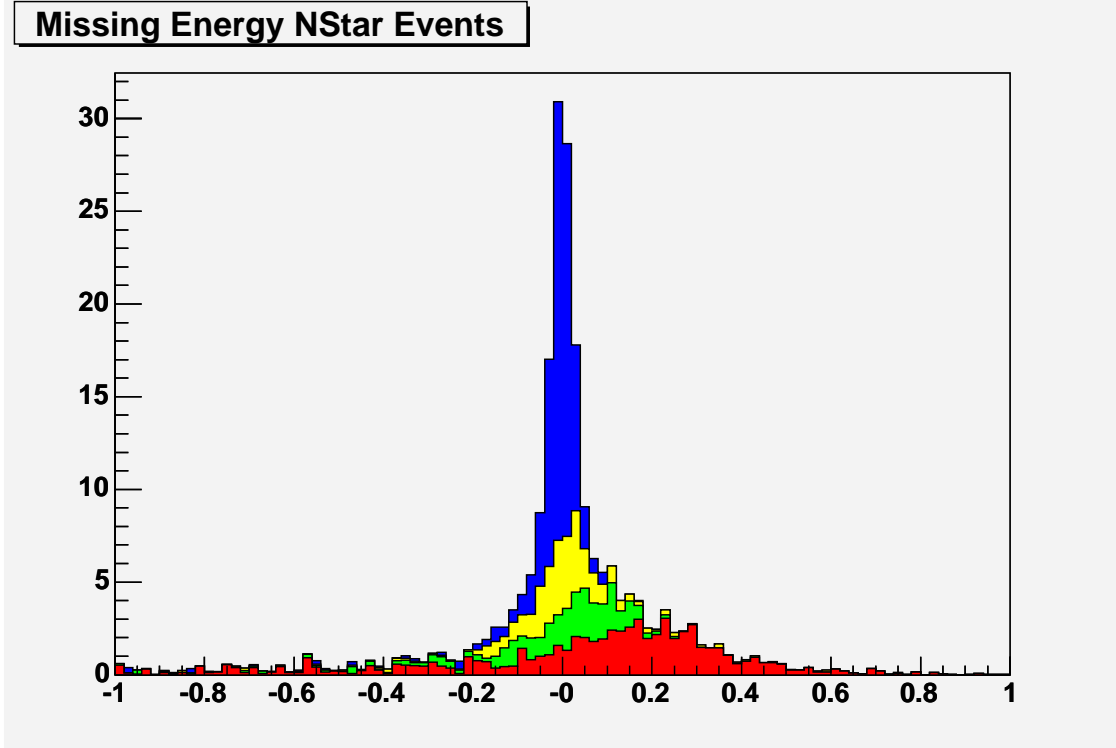


FIG. 8: Reconstructed missing energy $k_e + M - k' - q' - E_p$ in electron scattering kinematics of Fig. 9. The stacked histograms are from bottom to top: (Red) $ep \rightarrow eN^*\gamma$ events with the proton detected in the EndCap; (Green) N^* events with the proton in the Barrel; (Yellow) $ep \rightarrow ep\gamma$ exclusive events with the proton detected in the EndCap; and (Blue) exclusive events with the proton in the Barrel. The reconstruction algorithm is described in the text.

hour in the reaction $H(e, e'p)J/\Psi$. With at least 50% acceptance for each di-lepton decay channel, there will be 3 counts per hour in each di-lepton channel $H(e, e'pl^+l^-)$. Additional studies are needed to establish the resolution of J/Ψ reconstruction.

C. Conclusions

We have demonstrated that a very powerful detector can be built for deeply virtual exclusive reactions.

X. BIBLIOGRAPHY

- [1] D. Muller, *et al.*, *Fortsch. Phys.* **42**, 101 (1994).
- [2] X. Ji, *Phys. Rev. Lett.* **78**, 610 (1997).
- [3] A. V. Radyushkin, *Phys. Lett. B* **380**, 417 (1996).
- [4] J. C. Collins, L. Frankfurt and M. Strikman, *Phys. Rev. D* **56**, 2982 (1997).
- [5] M. Diehl, T. Gousset, B. Pire and J. P. Ralston, *Phys. Lett. B* **411**, 193 (1997).
- [6] A. V. Belitsky, D. Muller and A. Kirchner, *Nucl. Phys. B* **629**, 323 (2002).
- [7] M. Burkardt, *Phys. Rev. D* **66**, 114005 (2002).
- [8] M. Diehl, *Eur. Phys. J. C* **25**, 223 (2002); [Erratum-*ibid.* C **31**, 277 (2003)].
- [9] A.V. Belitsky, X. Ji and F. Yuan, *Phys. Rev. D* **69**, 074014 (2004).
- [10] E. R. Berger, M. Diehl and B. Pire, *Eur. Phys. J. C* **23**, 675 (2002).
- [11] R. Y. Zhu, D. A. Ma, H. B. Newman, C. L. Woody, J. A. Kierstad, S. P. Stoll and P. W. Levy, *Nucl. Instrum. Meth. A* **376**, 319 (1996).
- [12] S. Bachmann, A. Bressan, L. Ropelewski, F. Sauli and D. Mormann, *Nucl. Instrum. Meth. A* **433**, 464 (1999).

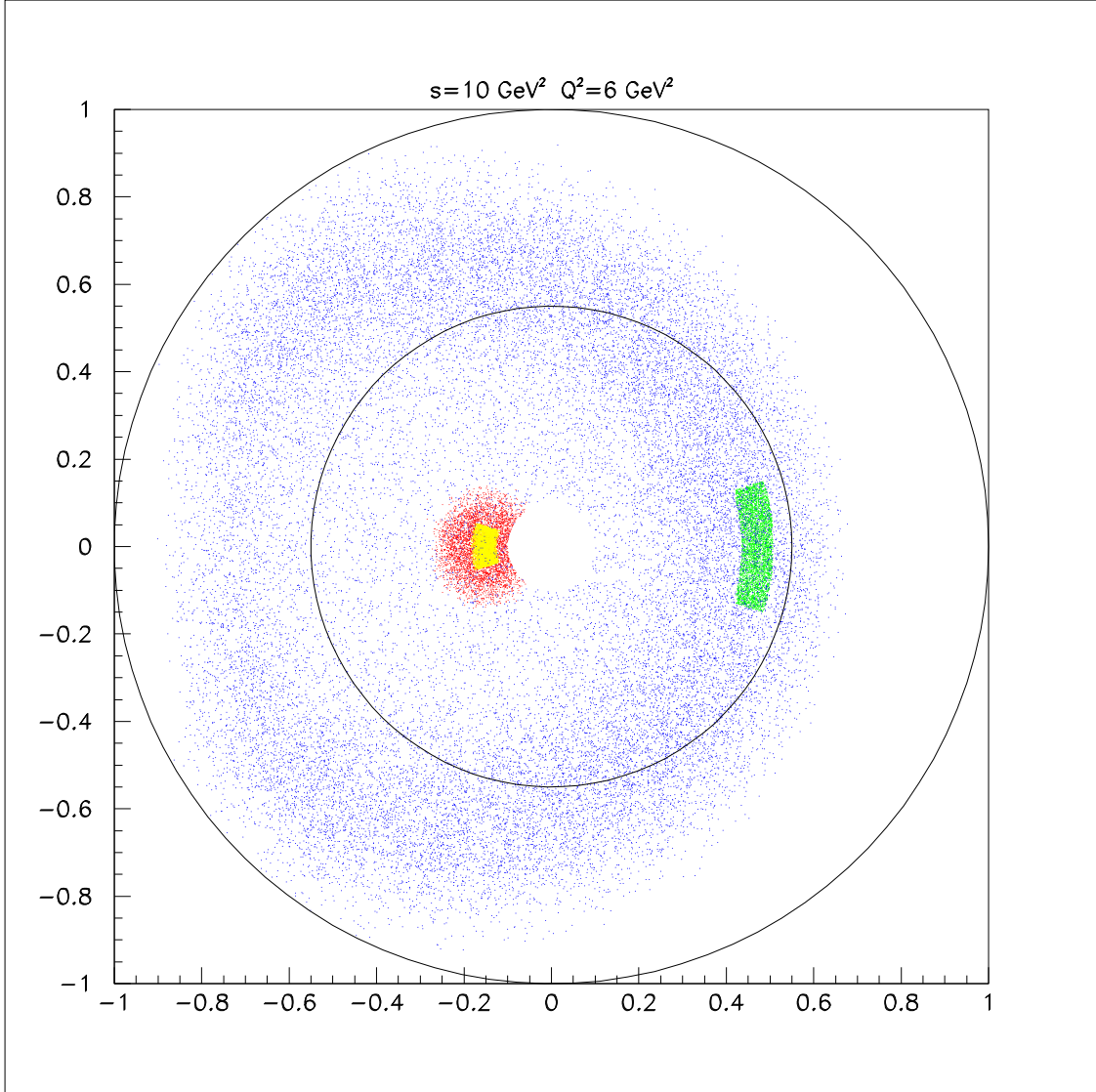


FIG. 9: Distribution of DVCS events on a plane 1 m downstream of the target. The electron kinematics are centered at $s = 10 \text{ GeV}^2$, $Q^2 = 6 \text{ GeV}^2$ at $k_e = 11 \text{ GeV}$. For clarity, the azimuthal angle of the electrons is truncated at ± 0.3 . The green cluster represents the scattered electrons, the yellow cluster the virtual photon direction, the red cluster the detected photons, and the blue dots the recoil protons. The generated events were limited to center-of-mass angles of the photon relative to the virtual photon of less than 30° . The circle at 0.55 m is the approximate limit of the EndCap Calorimeter. The circle at 1.0 m is the limit of the Barrel detectors for the protons.

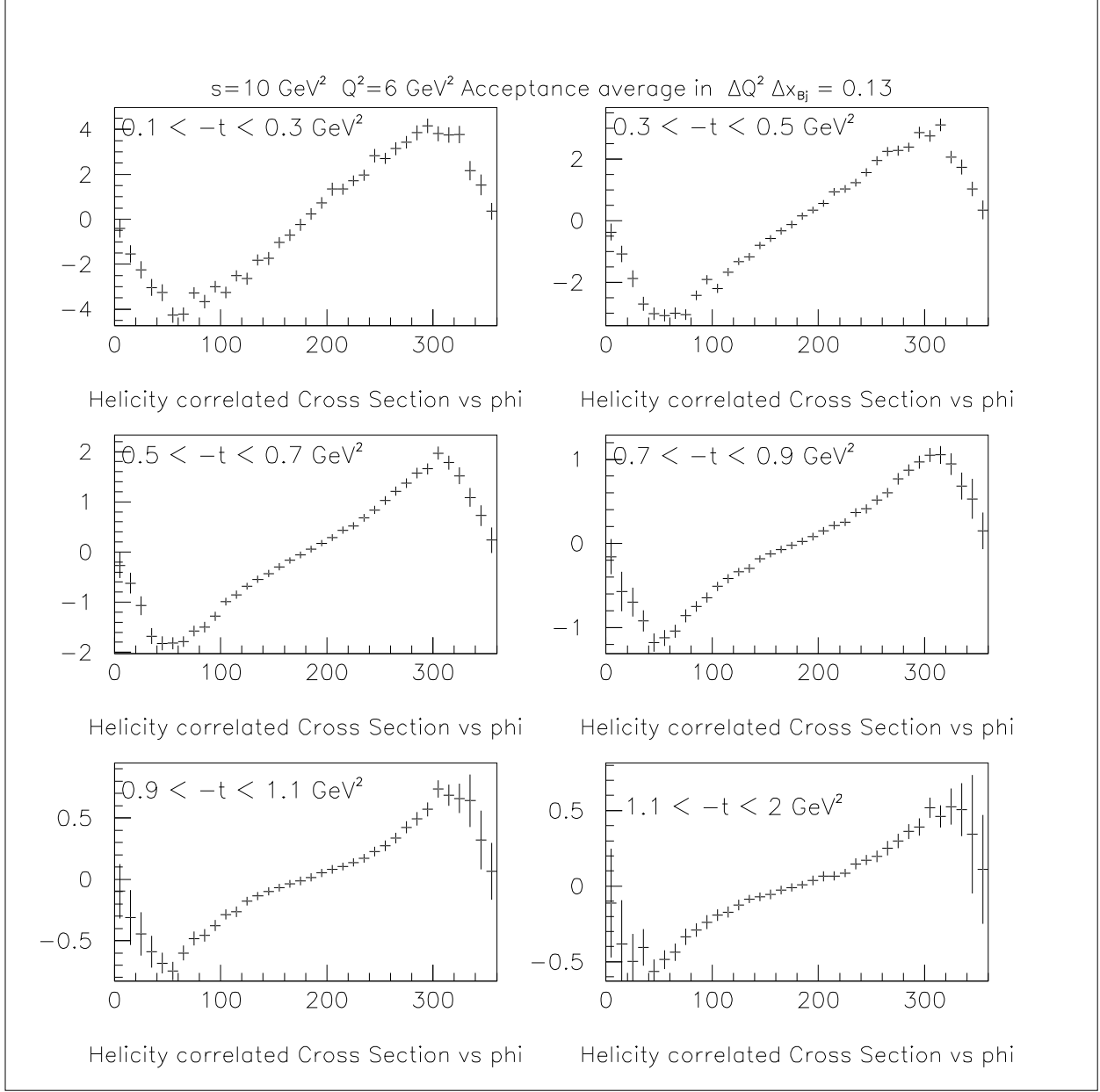


FIG. 10: Projected results, with statistical error bars, for the acceptance averaged helicity dependent cross section $d\Sigma/dk' d\Omega d\Omega_{\gamma\gamma}^{CM}$ (pb/GeV/sr²). The kinematics are the same as Fig. 9. The data are averaged over an electron scattering bin $d \cos \theta_e \otimes dk' = 0.06 \otimes 0.7 \text{ GeV}$, which corresponds to an average bin size of $\Delta Q^2 \Delta x_{Bj} = 0.13 \text{ GeV}^2$. The projected statistics are for 200 hours of beam with polarization 0.7 at the design luminosity $10^{37}/\text{cm}^2/\text{s}$.

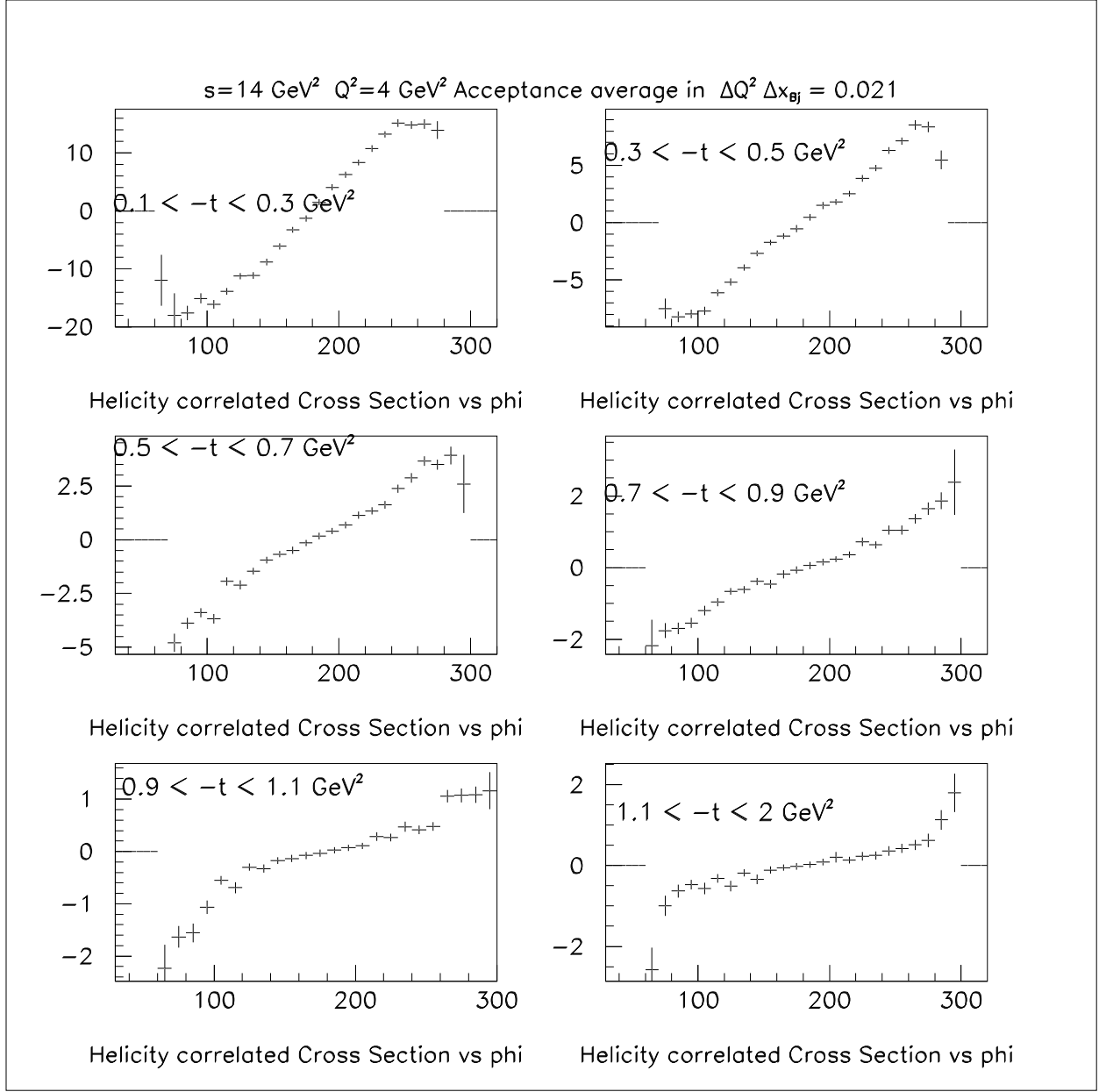


FIG. 11: Projected results, with statistical error bars, for the acceptance averaged helicity dependent cross section $d\Sigma/dk'd\Omega d\Omega_{\gamma\gamma}^{CM}$ (pb/GeV/sr²). The integrated luminosity and beam polarization are the same as Fig. 10. The data are averaged over an electron scattering bin of size $\Delta Q^2 \Delta x_{Bj} = 0.021 \text{ GeV}^2$. The kinematics are centered at $s = 14 \text{ GeV}^2$ and $Q^2 = 4 \text{ GeV}^2$ ($x_{Bj} = 0.23$).